PCCP

ROYAL SOCIETY OF CHEMISTRY

PAPER

View Article Online
View Journal

Cite this: DOI: 10.1039/d6cp00433d

Solubilization of PET in binary mixtures of HFIP and DCM

Md Arifuzzaman,[a] Jan-Michael Carrillo,[b] Bobby Sumpter,[b] Tomonori Saito[a] and Changwoo Do*[c]

Received 5th February 2026,
Accepted 1st May 2026

DOI: 10.1039/d6cp00433d

rsc.li/pccp

The dissolution of polyethylene terephthalate (PET) is a critical step for a solvent-based process, yet it typically requires highly corrosive or toxic solvents. Here, we investigate the solubilization and conformational behavior of PET in binary mixtures of hexafluoro-2-propanol (HFIP) and dichloromethane (DCM) as a strategy to reduce HFIP usage while maintaining effective dissolution. Small-angle neutron scattering (SANS) measurements reveal that PET remains molecularly dissolved in HFIP/DCM mixtures up to 50 vol% DCM. Analysis of PET chain conformations shows a transition from Gaussian behavior at low HFIP fractions to more swollen chains at intermediate compositions, accompanied by a counter-intuitive minimum in the radius of gyration at 50% HFIP. Complementary SANS measurements of the binary solvents demonstrate that compositional heterogeneity is maximized at this same solvent composition, suggesting a direct coupling between solvent microstructure and polymer dimensions. Molecular dynamics simulations corroborate the experimental findings, revealing solvent domain formation, preferential solvation of PET by HFIP, and a "caging" effect arising from solvent heterogeneity that leads to polymer coil compaction. Together, these results provide molecular-level insight into polymer behavior in mixed solvent systems and establish HFIP/DCM mixtures as a promising, more sustainable solvent platform for the PET post-process.

1 Introduction

Polyethylene terephthalate (PET) is one of the most widely used polymers due to its excellent strength, transparency, and toughness characteristics. These unique properties make PET an excellent material for textiles, photographic films, high-strength fibres, bottles, and packaging materials. However, waste plastic disposal and the environmental concerns present worldwide challenges in the public, academic, and commercial sectors. Although PET is the most recycled plastic by mechanical recycling, the majority of PET wastes are rejected due to additives, colors, mixed states, and other practical limitations.[1,2] Thus, even PET recycling remains low.[3] The degradation of PET is also challenging due to the inert nature of PET, which makes it resistant to microbial degradation and leads to a large accumulation of postconsumer PET waste, especially in oceans.[4,5] Growing concerns about the limitation of fossil reserves, environmental pollution, and the need for more efficient economies have highlighted the importance of repurposing and reprocessing PET.[6]

PET as one of the primary sources of waste plastics can be converted into useful and value-added products, such as fabric for clothing, plastic containers, automotive parts, and membrane filters through recycling. Mechanical recycling, solvolysis, pyrolysis, and gasification are some of the current methods used for plastic recycling. While solvent-based processes such as extraction and purification or post-modification of PET can provide alternative paths, poor solubility of PET often prevents re-purposing PET beyond these conventional recycling methods. Even in solvolysis-based chemical recycling, the process is typically heterogeneous due to the limited solubility of PET and requires full deconstruction to monomers due to limited solubility of deconstructed PET oligomers.

The dissolution of PET governs various processes such as reuse, modification, analysis, and intermediate steps during solvolysis. Access to true molecular dissolution, rather than heterogeneous swelling or partial solvation, is essential for enabling homogeneous post-modification reactions, fractionation, and advanced characterization of PET.[7,8] However, PET is soluble in a restricted range of organic solvents, most of which are corrosive or toxic, resulting in handling challenges. High solubility of PET is of great importance for providing paths for PET modification and reuse. Trifluoroacetic acid (TFA) and hexafluoro-2-propanol (HFIP) are known to be some of the

[a] Chemical Sciences Division, Oak Ridge National Laboratory, Oak Ridge, TN 37831, USA
[b] Center for Nanophase Materials Science, Oak Ridge National Laboratory, Oak Ridge, TN 37831, USA
[c] Neutron Scattering Division, Oak Ridge National Laboratory, Oak Ridge, TN 37831, USA. E-mail: doc1@ornl.gov

most effective solvent systems for solubilizing PET.[9,10] HFIP has been known to be a good solvent for synthetic chemistry for its potent hydrogen bonding abilities *via* the fluorine atoms, which is also a key characteristic for the good solubility of PET as well as for the applications in the green DES systems.[11,12] In terms of acidity, HFIP (pK_a = 9.23) is significantly less corrosive than TFA (pK_a = 0.23), and it can be used with steel equipment, an important consideration for future scale-up. PET can be quickly dissolved in pure TFA or HFIP at room temperature, leading to a colorless transparent solution. Other solvent systems used in the literature for PET are *o*-chlorophenol and *o*-cresol at temperatures of 80–90 °C, and sodium hydroxide glycol solutions near the boiling point (197 °C).[13] However, these systems are much less attractive, due to their toxicity and difficult handling.

While HFIP has demonstrated great potential for dissolving PET, HFIP alone is still far from being the best solvent choice for use in PET processing such as post-modification reactions. Less toxic and less reactive solvents are always desired. Here, we studied mixtures of dichloromethane (DCM) and HFIP in order to lower the use of HFIP while maintaining good solubility of PET. We expect that DCM's volatility and ability to dissolve a wide range of organic compounds will provide significant merits during the PET post-processes. To elucidate the microscopic origin of PET solubility in mixed HFIP/DCM solvents, small-angle neutron scattering (SANS) was employed. In contrast to small-angle X-ray scattering (SAXS), SANS provides strong and tunable contrast between the polymer and the surrounding solvents due to the large differences in neutron scattering length densities, enabling direct sensitivity to solvent organization and solvent–polymer correlations. This contrast sensitivity allows SANS to probe solvent heterogeneity and nanoscopic solvent structure around PET chains, which are central to understanding the role of mixed solvents in governing polymer conformation and solubility.

2 Experimental section

2.1 Materials

Laser+® W (L40A) polyethylene terephthalate (PET, M_w = 40 000 g mol^{-1}, intrinsic viscosity = 0.75 ± 0.02 dL g^{-1}, crystallinity >45%, T_m = 242 °C, bulk density = 1.35 g cm^{-3}) was supplied by DAK Americas and used as received. Dichloromethane (DCM) and hexafluoroisopropanol (HFIP) were purchased from Sigma Aldrich and used without further purification. All solvents were handled under ambient laboratory conditions.

Solvent mixtures were prepared by combining DCM and HFIP at defined volume ratios (DCM : HFIP = 70 : 30, 60 : 40, 50 : 50, 40 : 60, 20 : 80, 0 : 100) prior to PET addition. PET pellets were then added to the solvent or solvent mixture to achieve the desired polymer concentration. Samples were sealed and mixed under controlled conditions until homogeneous solutions were obtained. The specific DCM/HFIP ratios and PET concentrations investigated are detailed in the Results section.

All sample preparation steps were performed using clean, dry glassware to avoid contamination. Prepared samples were used directly for SANS measurements without further filtration or modification.

2.2 Small-angle neutron scattering (SANS)

SANS measurements were performed using an extended Q-range small-angle neutron scattering (EQ-SANS) instrument at the Spallation Neutron Source of Oak Ridge National Laboratory.[14,15] A single configuration was used for all measurements. A sample-to-detector distance of 4 m was used with a minimum wavelength setting of 2.5 Å and a chopper frequency of 60 Hz to cover a momentum transfer range of

$$0.01\ \text{Å}^{-1} < q < 0.3\ \text{Å}^{-1},$$

where

$$q = \frac{4\pi \sin(2\theta)}{\lambda}.$$

Here, 2θ is the scattering angle and λ is the neutron wavelength. All samples were loaded into quartz cuvettes from Hellma (Plainview, NY, USA) using syringes. Measured data were reduced following standard procedures, including corrections for detector sensitivity, solid angles, and dark currents.[16,17] Scattering intensities were placed on an absolute scale using a standard sample measurement of porous silica ($I(q = 0)$ = 450 cm^{-1}).[18]

2.3 Multiscale simulations

A model of PET consisted of a chain with 8 monomers. Interaction strengths between the PET model and HFIP and DCM were determined using quantum chemistry calculations. Specifically, the NWChem[19] suite of codes (version 7.0.2) was used to perform all-electron density functional theory (DFT) calculations with the hybrid meta functional m06-2x and the aug-cc-pvdz basis set. Full optimization of the PET–HFIP and PET–DCM systems was performed. The interaction energy was computed as the difference between the bound PET–HFIP and PET–DCM and their individual components. Likewise, interactions for DCM–HFIP, HFIP–HFIP, and DCM–DCM were calculated. The interaction energies (in units of kcal mol^{-1}) obtained from quantum chemistry calculations are tabulated in Table 1.

These energies were used for coarse-grained MD (CGMD) simulations of PET in the solvents by setting the PET–PET interaction strength as the reference energy, defined as ε in

Table 1 The interaction energy is defined as the difference between the bound energy of the A–B complex and the unbound energies of its components, reported in units of kcal mol^{-1} and ε, where ε = 8.73 kcal mol^{-1}

A–B	Interaction strength (kcal mol^{-1})	Interaction strength (ε)
PET–PET	8.73	1.00
PET–HFIP	34.0	3.89
PET–DCM	13.8	1.58
HFIP–HFIP	10.1	1.16
HFIP–DCM	4.1	0.47
DCM–DCM	3.6	0.41

reduced Lennard-Jones (LJ) units, while the remaining interactions were scaled relative to ε. For example, the PET–HFIP interaction is 34/8.73 = 3.89ε. In the CGMD simulations, a PET chain with degree of polymerization of 100 was connected *via* finite extensible nonlinear elastic (FENE) bonds and placed in a solution of LJ beads with characteristic size σ, with interaction strengths representing those of DCM and HFIP at different volume fractions. NPT equilibration at $P^* = 0.3$ was carried out for up to $10^4\tau$, where τ is the reduced time unit. The reduced temperature was set to $T^* = 1.0$, corresponding to a standard thermal condition in LJ simulations. This procedure allows the system density to relax to its equilibrium value prior to production runs. The production runs in the CGMD simulations were then performed in the canonical ensemble (NVT), where V is the average volume of the simulation box obtained from the NPT equilibration run, and the $\langle R_g^2 \rangle$ of the chain was calculated as a function of the HFIP volume fraction. To further validate the CGMD model and establish consistency with the all-atom simulations, we performed additional analyses presented in the SI (Fig. S1). These include comparisons of $\langle R_g^2 \rangle$ between all-atom and CGMD simulations, PET–HFIP and PET–DCM partial radial distribution functions, and scattering functions evaluated at different CGMD pressures. Together, these results demonstrate that the CGMD model captures the same underlying conformational and structural trends observed at the all-atom level. While a direct quantitative mapping between reduced-unit CGMD and experimental thermodynamic conditions is not possible, the simulations are designed to capture qualitative trends governed by relative interaction strengths rather than reproduce absolute experimental dimensions.

Concurrently, all-atom molecular dynamics simulations were done in the canonical (NVT) ensemble using LAMMPS.[20–22] The simulation box contained a single PET chain with 10 monomers in a solution of HFIP and DCM. Several simulation sets were prepared to cover different mole fractions of HFIP in the HFIP/DCM mixture. The initial configurations were generated following the procedure described elsewhere[23] in which the individual constituent molecules were built using the AVOGADRO software[24] and then randomly arranged in the box using PACKMOL.[25] The total system size was approximately 90 000 atoms. The GAFF forcefield parameters[26] were assigned following the procedure described in previous work.[23]

The simulation box was periodic in all directions, and isobaric–isothermal (NPT) ensemble simulations of up to 10 ns were performed to equilibrate the system. Temperature and pressure were controlled with a Nosé–Hoover thermostat and barostat, respectively, with the temperature set to 300 K and the pressure set to 1 atm. Long-range electrostatic interactions were evaluated using the FFT-based particle–particle/particle–mesh (PPPM) method, and a cutoff of 1 nm was applied to the van der Waals potential. The equations of motion were integrated with the velocity-Verlet scheme in LAMMPS using a timestep of 1 fs.

Following equilibration, production runs were carried out in the NVT ensemble at the equilibration dimensions obtained from the preceding NPT simulations. Each production run was continued for 100 ns, and trajectories were recorded every 5 ps.

3 Results and discussion

3.1 SANS

To visually confirm the solubility of PET, PET pellets were added to the solvents as shown in Fig. 1. After addition, the vials were vortex-mixed for several minutes at approximately 50 °C prior to observation. PET was not soluble in pure DCM under these conditions. In contrast, good solubility was observed in mixed solvents of 50 vol% DCM (HFIP : DCM = 1 : 1), as well as in pure HFIP.

PET solutions prepared in HFIP/DCM mixtures with HFIP volume fractions of 30, 40, 50, 60, 80, and 100% were measured using EQ-SANS at room temperature. Scattering contributions from the pure solvents were subtracted from the measured intensities. Scattering contrast arises from the difference in scattering length density (SLD) between PET (2.59×10^{-6} Å^{-2}) and DCM (1.78×10^{-6} Å^{-2}), whereas the SLD of HFIP (2.99×10^{-6} Å^{-2}) is close to that of PET (Fig. 2a). As the HFIP fraction increases beyond 60%, the SLD of the mixed solvent approaches that of PET, causing the coherent scattering signal from the polymer to nearly disappear (Fig. 2b).

The coherent scattering intensities shown in Fig. 2a were analyzed using a polymer chain form factor with excluded-volume effects,[27,28]

$$I(q) = I_0 \left[\frac{1}{\nu U^{1/2\nu}} \gamma\left(\frac{1}{2\nu}, U\right) - \frac{1}{\nu U^{1/\nu}} \gamma\left(\frac{1}{\nu}, U\right) \right] + b_{\mathrm{inc}}, \quad (1)$$

where ν is the excluded-volume parameter related to the Porod exponent m by $\nu = 1/m$, b_{inc} is the incoherent background, and $\gamma(x,U)$ is the incomplete gamma function,

$$\gamma(x, U) = \int_0^U \mathrm{e}^{-t} t^{x-1} \mathrm{d}t. \quad (2)$$

The variable U is related to the radius of gyration R_g through

$$U = \frac{q^2 R_g^2 (2\nu + 1)(2\nu + 2)}{6}. \quad (3)$$

For PET solutions containing 30, 40, and 50% HFIP, the scattering data could be reasonably described by this model (Fig. 2a, solid lines). However, equally good fits were obtained over a broad range of Porod exponents ($1.7 < m < 3$), corresponding to conformations ranging from swollen coils ($m \approx 5/3$) to globular structures ($m \approx 3$), including ideal Gaussian chains

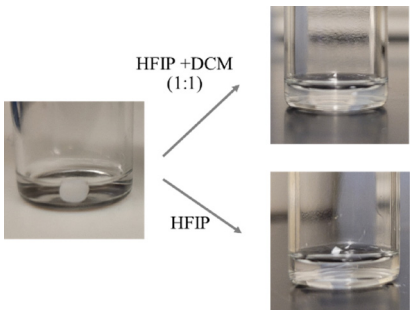

Fig. 1 Photographs of a PET pellet in DCM, HFIP, and mixed solvent.

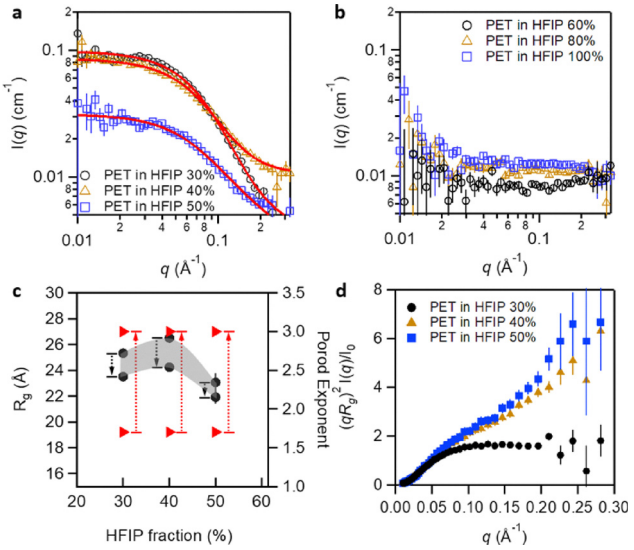

Fig. 2 Measured SANS intensities from the PET dissolved in HFIP:DCM solvent with various fractions of HFIP. (a) Scattering intensities with strong coherent signal were analyzed with a polymer chain model fit. (b) As the HFIP fraction increases, PET loses its scattering contrast in the solvent and coherent scattering signal from the PET structure disappears. (c) R_g (solid circle, left axis) obtained from the fitting varies depending on the choice of the Porod exponents (solid triangle, right axis). The quality of fit shown in (a) does not change regardless of the value of the Porod exponent within this range. Arrows with dotted line show the direction of change as the Porod exponent is varied from 1.7 to 3. (d) Kratky plot of measured data (a).

($m \approx 2$). The resulting ranges of fitted R_g values are shown in Fig. 2c as a function of the fixed Porod exponent. Increasing the Porod exponent leads to a slight decrease in the extracted R_g values. The shaded region in Fig. 2c illustrates the overall trend of R_g with increasing HFIP fraction.

Although HFIP is generally recognized as a good solvent for PET, a counter-intuitive minimum in R_g is observed at 50% HFIP, where the estimated R_g is smaller than that obtained at lower HFIP fractions. This non-monotonic behavior highlights the complex nature of polymer conformations in mixed solvent systems, which can differ substantially from single-component solvents due to asymmetric interactions between the polymer and each solvent component, as well as interactions between the solvent components themselves. Phenomena such as preferential solvation and cononsolvency, in which mixtures of two good solvents act effectively as poor solvents, can lead to polymer coil compaction.[29–31] It is also worth noting that this effect depends on polymer concentration,[32] with qualitatively different behavior observed between dilute solution and polymer-rich (thin-film) regimes. Our system lies in the dilute regime.

Further insight into the polymer conformation is obtained from the Kratky representation shown in Fig. 2d. For PET dissolved in 30% HFIP, a plateau is observed at large q, consistent with Gaussian chain behavior. In contrast, PET solutions at 40 and 50% HFIP show positive deviations from the plateau at high q, indicating increased excluded-volume effects and locally swollen chain conformations. The apparent discrepancy between the locally swollen behavior indicated by

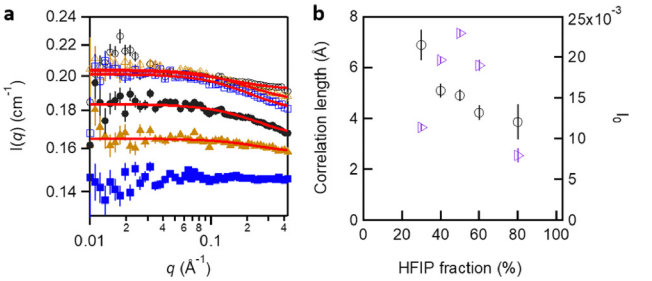

Fig. 3 (a) SANS intensities of binary liquids, HFIP and DCM at various volume fractions of HFIP: 30% (open circles), 40% (open triangles), 50% (open squares), 60% (solid circles), 80% (solid triangles), and 100% (solid squares). (b) Correlation lengths (ξ, circles) and I_0 (triangles) obtained from the model fit.

the Kratky plots and the reduced global R_g at 50% HFIP suggests that solvent-induced structural heterogeneity leads to global chain compaction despite enhanced local flexibility.

To elucidate the role of solvent microstructure, SANS measurements of the binary HFIP/DCM solvents were performed. Fig. 3a shows that, unlike the pure solvents, which exhibit nearly flat scattering profiles, the binary HFIP/DCM mixtures display enhanced scattering at high q, indicating the presence of solvent microstructures or composition fluctuations. Scattering intensities arising from spatial fluctuations in composition and density were analyzed using the Ornstein–Zernike model,

$$I(q) = \frac{I_0}{1 + q^2\xi^2} + b_{\mathrm{inc}}, \tag{4}$$

where ξ is the correlation length and b_{inc} is the incoherent background. The measured data, fitted curves, and extracted parameters are shown in Fig. 3.

In Fig. 3b, the correlation length decreases monotonically with increasing HFIP fraction, indicating that the characteristic size of compositional fluctuations becomes smaller as HFIP content increases. Notably, the forward scattering intensity I_0 reaches a maximum at 50% HFIP. This behavior implies that while the domain size decreases, the number or contrast of compositional fluctuations is maximized at this composition. Importantly, this maximum in solvent heterogeneity coincides with the minimum in PET R_g, suggesting a direct coupling between solvent microstructure and polymer dimensions. Enhanced solvent heterogeneity at 50% HFIP effectively restricts polymer expansion, resulting in a more compact coil conformation.

3.2 Multiscale simulations

Similar to the SANS experiments, the coarse-grained molecular dynamics (CGMD) simulations exhibit a non-monotonic dependence of $\langle R_g^2 \rangle$ on the HFIP volume fraction. As shown in Fig. 4, $\langle R_g^2 \rangle$ increases from 0 to 0.25 HFIP fraction, then exhibits oscillatory behavior, reaching its maximum in pure HFIP, consistent with HFIP being a good solvent for PET. The characteristic time was obtained from the autocorrelation function of $\langle R_g^2 \rangle$, and error bars were estimated as the standard error of the mean using block averaging, confirming that the

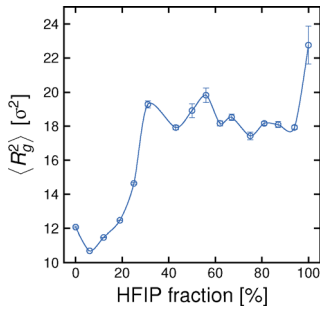

Fig. 4 Dependence of the mean-square radius of gyration, $\langle R_g^2 \rangle$, on the HFIP fraction in the solvent matrix obtained from CGMD simulations.

0.25, 0.5, and 0.75 HFIP cases are statistically distinct. While the precise HFIP fraction at which the local maximum occurs differs between the SANS (Fig. 3b) and CGMD data, both methods qualitatively agree in demonstrating non-monotonic behavior. However, this dependence is less clearly resolved in the all-atom MD simulations due to large error bars, even with block averaging (see Fig. S1a in the SI), as the simulated PET chain is relatively short (10 monomers).

To rationalize the non-monotonic behavior of $\langle R_g^2 \rangle$ as a function of HFIP volume fraction in the CGMD simulations, the interaction energies reveal the hierarchy HFIP–HFIP > DCM–HFIP > DCM–DCM. For pure DCM, which is a poorer solvent for PET than HFIP, the chain exhibits the smallest $\langle R_g^2 \rangle$. Adding a small amount of HFIP improves the local environment because HFIP–DCM interactions are more favorable than DCM–DCM, and preferential adsorption of HFIP onto PET swells the chain, leading to an increase in $\langle R_g^2 \rangle$ at low HFIP concentrations, up to a maximum. As the HFIP concentration increases further, stronger HFIP self-association drives the formation of HFIP-rich clusters, depleting the PET solvation shell of HFIP and enriching it with DCM. This worsens the effective solvent quality and reduces $\langle R_g^2 \rangle$ to a local minimum. At high HFIP concentrations, however, there is enough HFIP to overcome self-association and saturate the PET solvation shell, and the polymer size reaches a global maximum in pure HFIP.

Although the CGMD simulations capture the expected qualitative behavior based on interaction energies from quantum chemistry calculations, the all-atom MD simulations provide visual evidence of the solvent internal structure and heterogeneity at different HFIP : DCM ratios at atomic resolution. As shown in Fig. 5, distinct inhomogeneities and the formation of solvent domains are observed within the binary mixtures, corroborating the experimental SANS results indicating significant compositional fluctuations in the microstructure of the binary liquids. We also note that the coarse-grained and all-atom simulations are not intended to quantitatively reproduce the absolute experimental R_g values, but rather to isolate interaction hierarchies and solvent structural effects governing qualitative conformational trends.

The ability of MD to visualize dynamic solvent arrangements is critical to understand how the local environment around the polymer chain is influenced by the overall solvent composition. Fig. 6 shows calculated scattering functions from the binary solvent mixtures, where the weight of each atom in an HFIP molecule is set to 1.0 and all others to zero. The correlation length in the binary mixtures was obtained from these curves using the Ornstein–Zernike equation, in the same manner as was applied in fitting the experimental data. These correlation length values, which are directly related to the characteristic size of solvent-rich domains, decrease with increasing HFIP concentration (Fig. 7a). This trend is consistent with the experimental SANS results for the binary solvent mixtures, where the correlation length also decreases monotonically with increasing HFIP fraction (Fig. 3).

Beyond the scattering-curve analysis, the MD simulations also provide quantitative information on the population of solvent microdomains through the cluster-density analysis shown in Fig. 7b. At low HFIP fractions, HFIP is present as numerous

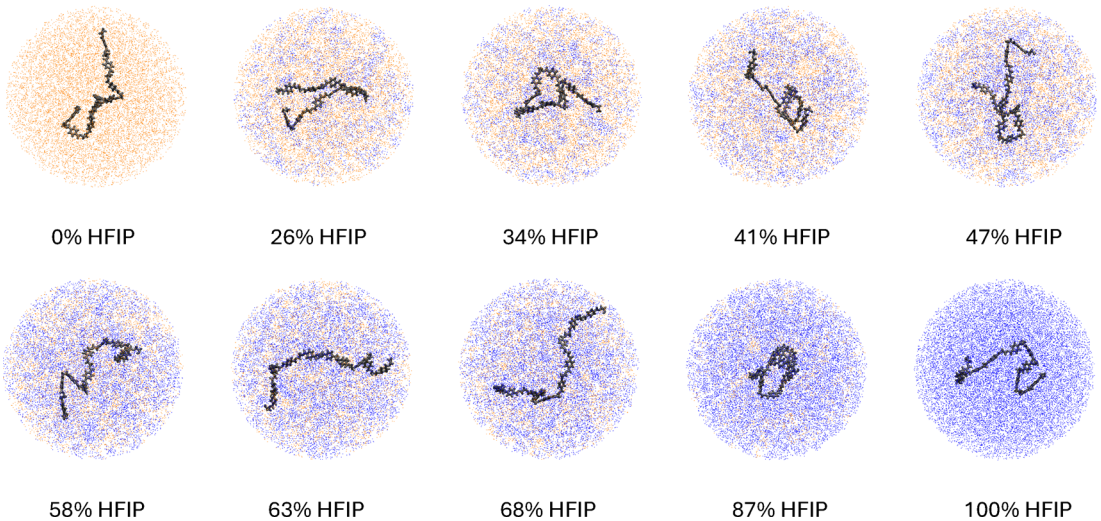

Fig. 5 All-atom MD simulation snapshots of a single PET chain (gray) in solvents consisting of HFIP (blue) and DCM (orange) at different HFIP volume fractions.

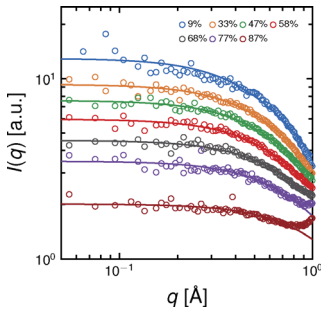

Fig. 6 Scattering function of binary liquids consisting of HFIP and DCM, with the scattering length density set to one for atoms in HFIP molecules and zero otherwise, at different HFIP volume fractions calculated from all-atom MD simulations. The lines represent fits using the Ornstein–Zernike equation.

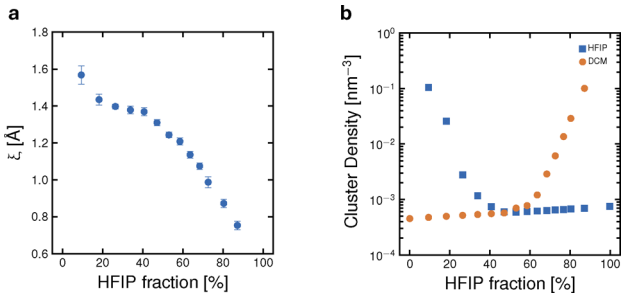

Fig. 7 (a) Correlation length (ξ) of HFIP/DCM binary mixtures obtained from fits to the Ornstein–Zernike equation, based on all-atom MD simulations at different HFIP volume fractions. (b) Number density of HFIP (blue) and DCM (orange) clusters as a function of HFIP volume fraction, obtained from all-atom MD simulations.

isolated HFIP-rich clusters dispersed in a DCM-rich matrix, giving a relatively high HFIP cluster density. As the HFIP fraction increases, these HFIP-rich clusters progressively merge into a more continuous HFIP-rich environment, leading to a decrease in HFIP cluster density. In contrast, the DCM cluster density remains comparatively low over the intermediate composition range but increases sharply at high HFIP fractions, where DCM becomes the minority component and forms isolated DCM-rich domains within the HFIP-rich matrix. This inversion in the dominant dispersed phase highlights the strongly composition-dependent nature of the solvent microstructure. Importantly, the intermediate composition range, where neither solvent forms a completely homogeneous environment, coincides with the regime in which PET exhibits anomalous conformational behavior. Thus, Fig. 7b supports the interpretation that local composition fluctuations and transient solvent domains modify the effective solvation environment around PET, contributing to the solvent-mediated confinement or the ''caging'' effect responsible for the compact chain conformation.

4. Conclusions

In this work, we investigated the dissolution and conformational behavior of polyethylene terephthalate (PET) in binary mixtures of hexafluoro-2-propanol (HFIP) and dichloromethane (DCM) by combining small-angle neutron scattering (SANS) experiments with multiscale molecular dynamics simulations. The results demonstrate that PET can be effectively dissolved in HFIP/DCM mixtures containing up to 70 vol% DCM, enabling a significant reduction in HFIP usage while maintaining molecular-level solubility. SANS measurements reveal a non-monotonic dependence of the PET radius of gyration on the HFIP fraction, with a counter-intuitive minimum at approximately 50% HFIP, indicating that polymer conformation in mixed solvents cannot be inferred from single-solvent quality alone.

Complementary SANS measurements of the binary solvents show that compositional heterogeneity is maximized at the same solvent composition where the minimum in the PET radius of gyration is observed, establishing a direct experimental link between solvent microstructure and polymer dimensions. Multiscale simulations provide molecular-level insight into this behavior and strongly support the experimental findings. Both coarse-grained and all-atom MD simulations reproduce the non-monotonic trend in polymer size and reveal pronounced solvent inhomogeneities and domain formation in HFIP/DCM mixtures. Calculated scattering functions from the simulated solvent mixtures yield correlation lengths that decrease with increasing HFIP fraction, in excellent agreement with experimental SANS results.

Analysis of intermolecular interactions from the simulations shows strong preferential solvation of PET by HFIP through hydrogen bonding, while DCM interacts more weakly. At intermediate compositions, particularly near 50% HFIP, competition between preferential solvation and HFIP self-association leads to enhanced solvent heterogeneity, which effectively ''cages'' the PET chain and produces a more compact global conformation despite locally favorable polymer–solvent interactions. Together, the experimental and simulation results consistently demonstrate that solvent microstructure plays a decisive role in governing polymer conformation in mixed solvent systems and provide clear design principles for developing efficient and environmentally benign solvent platforms for PET processing.

Author contributions

Changwoo Do contributed to conceptualization, methodology, experimental investigation (SANS), data analysis, and writing – original draft. Md Arifuzzaman contributed to materials preparation, characterization, investigation, and writing – review & editing. Jan-Michael Carrillo contributed to simulation methodology, molecular dynamics simulations, data analysis, and writing – review & editing. Bobby Sumpter contributed to simulation conceptualization, supervision, interpretation of simulation results, and writing – review & editing. Tomonori Saito contributed to conceptualization, project initiation, supervision, funding acquisition, and writing – review & editing. All authors contributed to manuscript preparation and approved the final version.

Conflicts of interest

There are no conflicts to declare.

Data availability

Data for this article, including SANS scattering data, processed datasets, and analysis scripts supporting the experimental results, are available at the Open Science Framework (OSF) repository at https://doi.org/10.17605/OSF.IO/XAFE9. Simulation input files and representative trajectories supporting the molecular dynamics results are also available at this repository. Additional data that support the findings of this study but are not included in the repository are available from the corresponding author upon reasonable request.

Supplementary information is available. See DOI: https://doi.org/10.1039/d6cp00433d.

Acknowledgements

This research was supported by the U.S. Department of Energy, Office of Science, Basic Energy Sciences, Materials Sciences and Engineering Division. This research used resources at the Spallation Neutron Source, a DOE Office of Science User Facility operated by the Oak Ridge National Laboratory. The beam time was allocated to EQ-SANS on proposal number IPTS-31821. The computational portion of this work was performed at the Center for Nanophase Materials Sciences, a US Department of Energy Office of Science User Facility operated at Oak Ridge National Laboratory. This research used resources of the Oak Ridge Leadership Computing Facility (OLCF) at the Oak Ridge National Laboratory, which is supported by the Office of Science of the U.S. Department of Energy under Contract No. DE-AC05-00OR22725.

Notes and references

1 I. Vollmer, M. J. Jenks, M. C. Roelands, R. J. White, T. Van Harmelen, P. De Wild, G. P. van Der Laan, F. Meirer, J. T. Keurentjes and B. M. Weckhuysen, *Angew. Chem., Int. Ed.*, 2020, **59**, 15402–15423.
2 N. A. Rorrer, S. Nicholson, A. Carpenter, M. J. Biddy, N. J. Grundl and G. T. Beckham, *Joule*, 2019, **3**, 1006–1027.
3 J. Zheng, M. Arifuzzaman, X. Tang, X. C. Chen and T. Saito, *Mater. Horiz.*, 2023, **10**, 1608–1624.
4 D. Kint and S. Muñoz-Guerra, *Polym. Int.*, 1999, **48**, 346–352.
5 R. J. Müller, I. Kleeberg and W. D. Deckwer, *J. Biotechnol.*, 2001, **86**, 87–95.
6 F. Awaja and D. Pavel, *Eur. Polym. J.*, 2005, **41**, 1453–1477.
7 Z. Xu, K. Sanchez-Rivera, C. Granger, P. Zhou, A. D. C. Munguia-Lopez, U. M. Ikegwu, S. Avraamidou, V. M. Zavala, R. C. Van Lehn and E. Bar-Ziv, *et al.*, *Nat. Chem. Eng.*, 2025, **2**, 407–423.
8 G. W. Coates and Y. D. Getzler, *Nat. Rev. Mater.*, 2020, **5**, 501–516.
9 W. W. Deng, Y. Zong and Y. X. Xiao, *ACS Sustainable Chem. Eng.*, 2017, **5**, 4267–4275.
10 S. B. Lawrenson, R. Arav and M. North, *Green Chem.*, 2017, **19**, 1685–1691.
11 I. Colomer, A. E. R. Chamberlain, M. B. Haughey and T. J. Donohoe, *Nat. Rev. Chem.*, 2017, **1**, 0088.
12 J. Xu, Y. Yang, X. Cai and H. Xiao, *RSC Adv.*, 2023, **13**, 9595–9606.
13 S. S. Karim, S. Farrukh, T. Matsuura, M. Ahsan, A. Hussain, S. Shakir, L. F. Chuah, M. Hasan and A. Bokhari, *Chemosphere*, 2022, **307**, 136050.
14 J. K. Zhao, C. Y. Gao and D. Liu, *J. Appl. Crystallogr.*, 2010, **43**, 1068–1077.
15 W. T. Heller, M. Cuneo, L. Debeer-Schmitt, C. Do, L. He, L. Heroux, K. Littrell, S. V. Pingali, S. Qian, C. Stanley, V. S. Urban, B. Wu, W. Bras and IUCr, *J. Appl. Crystallogr.*, 2018, **51**, 242–248.
16 O. Arnold, J. Bilheux, J. Borreguero, A. Buts, S. Campbell, L. Chapon, M. Doucet, N. Draper, R. Ferraz Leal, M. Gigg, V. Lynch, A. Markvardsen, D. Mikkelson, R. Mikkelson, R. Miller, K. Palmen, P. Parker, G. Passos, T. Perring, P. Peterson, S. Ren, M. Reuter, A. Savici, J. Taylor, R. Taylor, R. Tolchenov, W. Zhou and J. Zikovsky, *Nucl. Instrum. Methods Phys. Res., Sect. A*, 2014, **764**, 156–166.
17 W. T. Heller, J. Hetrick, J. Bilheux, J. M. B. Calvo, W.-R. Chen, L. DeBeer-Schmitt, C. Do, M. Doucet, M. R. Fitzsimmons, W. F. Godoy, G. E. Granroth, S. Hahn, L. He, F. Islam, J. Lin, K. C. Littrell, M. McDonnell, J. McGaha, P. F. Peterson, S. V. Pingali, S. Qian, A. T. Savici, Y. Shang, C. B. Stanley, V. S. Urban, R. E. Whitfield, C. Zhang, W. Zhou, J. J. Billings, M. J. Cuneo, R. M. F. Leal, T. Wang and B. Wu, *SoftwareX*, 2022, **19**, 101101.
18 G. T. Wignall and F. Bates, *Appl. Crystallogr.*, 1987, **20**, 28–40.
19 E. Apra, E. J. Bylaska, W. A. De Jong, N. Govind, K. Kowalski, T. P. Straatsma, M. Valiev, H. J. van Dam, Y. Alexeev and J. Anchell, *et al.*, *J. Chem. Phys.*, 2020, **152**, 184102.
20 A. P. Thompson, H. M. Aktulga, R. Berger, D. S. Bolintineanu, W. M. Brown, P. S. Crozier, P. J. In't Veld, A. Kohlmeyer, S. G. Moore and T. D. Nguyen, *et al.*, *Comput. Phys. Commun.*, 2022, **271**, 108171.
21 W. M. Brown, P. Wang, S. J. Plimpton and A. N. Tharrington, *Comput. Phys. Commun.*, 2011, **182**, 898–911.
22 S. Plimpton, *J. Comput. Phys.*, 1995, **117**, 1–19.
23 D. Chang, M. Lorenz, M. J. Burch, O. S. Ovchinnikova, K. Hong, B. G. Sumpter and J.-M. Y. Carrillo, *ACS Appl. Polym. Mater.*, 2019, **2**, 209–219.
24 M. D. Hanwell, D. E. Curtis, D. C. Lonie, T. Vandermeersch, E. Zurek and G. R. Hutchison, *J. Cheminf.*, 2012, **4**, 17.
25 L. Martínez, R. Andrade, E. G. Birgin and J. M. Martínez, *J. Comput. Chem.*, 2009, **30**, 2157–2164.
26 J. Wang, R. M. Wolf, J. W. Caldwell, P. A. Kollman and D. A. Case, *J. Comput. Chem.*, 2004, **25**, 1157–1174.

27 J. S. Higgins and H. C. Benoit, *Polymers and Neutron Scattering*, Oxford University Press, New York, 1994.
28 B. Hammouda, *Adv. Polym. Sci.*, 1993, **106**, 87–133.
29 A. R. Shultz and P. J. Flory, *J. Polym. Sci.*, 1955, **15**, 231–242.
30 X. Zhang, J. Zong and D. Meng, *Soft Matter*, 2020, **16**, 7789.
31 S. Bharadwaj, B.-J. Niebuur, K. Nothdurft, W. Richtering, N. F. A. van der Vegt and C. M. Papadakis, *Soft Matter*, 2022, **18**, 2873–2898.
32 L. P. Kreuzer, C. Lindenmeir, C. Geiger, T. Widmann, V. Hildebrand, A. Laschewsky, C. M. Papadakis and P. Muller-Buschbaum, *Macromolecules*, 2021, **54**, 1548–1556.